Backscatter Distributions of Persistent and Distributed Scatterers Over Wavelength: Results From *X*-, *C*-, and *L*-Band

Stacey Huang, *Student Member, IEEE*, and Howard A. Zebker, *Life Fellow, IEEE*

***Abstract*—Persistent scatterer (PS) techniques are a set of important time-series tools for interferometric synthetic aperture radar (InSAR) that enable deformation analysis in highly decorrelated terrain. Detailed knowledge of the statistics of persistent scatterers in InSAR images is critical for the design of better techniques that will enable both the extraction of deformation in traditionally difficult regions as well as develop a better understanding of how performance of these algorithms relates to important system parameters. In this article, we characterize the backscatter statistics of both persistent and distributed scatterers over wavelength using data from *X*-band (COSMO-SkyMed), *C*-band (Sentinel-1), and *L*-band (ALOS) sensors. We show that popular distributions that have previously been used to fit SAR backscatter can effectively capture the returns from both PS and clutter, with the G^0 distribution being the most applicable across wavelength and scatterer type. Thus, our work paves the way for improved detection algorithms to be designed based on these distributions and also builds an initial foundation for developing a greater theoretical understanding of PS statistics.**

***Index Terms*—Interferometric synthetic aperture radar (InSAR), persistent scatterers (PSs), wavelength.**

I. Introduction

INTERFEROMETRIC synthetic aperture radar (InSAR) has become an increasingly popular remote sensing tool for geophysical and earth-observing studies [1], [2]. Advanced satellite development in recent years has increased the applicability of the technique due to improvements in satellite resolution and more frequent revisit times, enabling more precise scientific studies and frequent time-sensitive applications such as damage assessment [3]. However, InSAR studies of many important natural regions, such as forested and vegetated terrain, are often still limited due to difficulties in extracting reliable deformation signals in areas that suffer from high decorrelation [4].

Persistent scatterer (PS) interferometry is one widely implemented technique for studying rapidly decorrelating regions in InSAR [5], [6]. PSs are temporally stable pixels in an InSAR image that can be used to form a reliable network of points which can then be used for analysis. By applying this technique, we can analyze ground deformation of several millimeters in areas that otherwise suffer from high decorrelation. PS interferometry has been applied to applications as diverse as urban building characteristics, subsidence in cities, volcanic activity, and landslide dynamics [7]–[10].

While current analytical methods have proven effective in detecting PS and exploiting their desirable properties, the development of these algorithms has primarily been driven by empirical observations. Notably, previous studies have already noted the importance of quantities such as wavelength [11] and image resolution [12] on PS density. However, there are few published studies that study these phenomena in detail and that address the theoretical understanding of PS statistics and its relation to system parameters. Such research and a suitable theoretical framework are needed for the design of increasingly accurate and analytically sound detection methods, which in turn would result in a denser network of reliable measurements that enable more detailed deformation analysis.

In this article, we present initial results from analysis of the statistics of PS and distributed scatterers (clutter) as a function of wavelength. In Section II, we outline the theoretical basis for modeling PS statistics and why backscatter distributions are of interest. In Section III, we describe our test dataset. In Section IV, we examine distributions that fit to the power backscatter of both scatterer types and show that we can model both PS and clutter with the G^0 distribution. We discuss possible other factors that may contribute to differing observed statistics by satellite, and we conclude with general observations and suggestions for next steps.

II. Characterization and Detection of PS

Over the years, a wide variety of PS detection methods has been developed [13], [14]. These detection methods can generally be grouped by the type of measure used to characterize and analyze PS statistics—amplitude-based (including amplitude dispersion and the signal-to-clutter ratio), coherence, statistical homogeneity, and spectral diversity. For this work, we choose to develop our model based on estimating the signal-to-clutter ratio of each pixel (denoted SCR or γ), which is utilized in techniques such as the spatio-temporal unwrapping network algorithm [15]

Manuscript received February 28, 2020; revised August 18, 2020; accepted September 11, 2020. Date of publication September 15, 2020; date of current version October 7, 2020. This work was supported in part by the National Science Foundation Graduate Research Fellowship Program under Grant DGE-1656518 and in part by the Sequoia Capital Fellowship from Stanford University. *(Corresponding author: Stacey Huang.)*

Stacey Huang is with the Electrical Engineering Department, Stanford University, Stanford, CA 94305 USA (e-mail: sahuang@stanford.edu).

Howard A. Zebker is with the Electrical Engineering and Geophysics Department, Stanford University, Stanford, CA 94305 USA (e-mail: zebker@stanford.edu).

Digital Object Identifier 10.1109/JSTARS.2020.3024174

and the maximum likelihood estimation (MLE) method [16]. PS are then selected as the pixels with an estimated SCR above a certain threshold. Previous research has found that higher SCR, which describes the strength of the dominant scatterer with respect to the clutter in a resel, corresponds to lower phase uncertainty [17]. While the method is simple, it serves as starting point for understanding PS statistics and can easily be extended to more complex analysis methods.

Following [18], we define the signal-to-clutter ratio (γ or SCR) as

$$\gamma = \frac{P_d}{P_c + P_n} \tag{1}$$

where P_d is the backscattered power from one or multiple dominant scatterers in one resolution element ("resel,") P_c is the power from clutter, and P_n is the power contribution of thermal noise. (1) is an important formulation to consider when taking into account bandwidth effects on PS density, as thermal noise is bandwidth-dependent.

We assume that due to spatial and temporal fluctuations in the radar cross section (RCS) and other noise sources, P_d and P_c can be taken as random variables. P_n is also commonly modeled as a random variable, usually exponential. Therefore, this equation suggests that with knowledge of the power distributions of PS and clutter, we can describe the statistics of γ and optimize detection algorithms accordingly. Thus, we would like to better understand how to model P_d and P_c and whether a unifying distribution over varying system parameters—namely, wavelength, can be used to describe them.

Previous InSAR and PS analyses have traditionally relied on the assumption that radar backscatter is distributed according to a complex bivariate Gaussian distribution, due to the tractability of the model [19], [20]. However, Gaussian statistics have long been recognized to be oversimplifications of high-resolution SAR statistics, and early data have shown that the amplitude of radar backscatter exhibits distributions with long tails that the Rayleigh distribution is unable to model [21]–[25]. As a result, various other distributions have been employed and designed over the years to describe SAR amplitude backscatter, including the Weibull, K, G, GC, G^0, and generalized Rayleigh distributions, among others [26]–[28]. Many of these distributions of SAR statistics are based on the idea that the SAR backscatter is composed of a two components: a texture (modulation) component and a speckle component, which acts as multiplicative noise [25], [27]. Thus, this assumes that we can describe the backscatter of a SAR image as follows:

$$\tilde{A} = \tilde{A}_t \cdot \tilde{A}_s \tag{2}$$

where A_t describes the contribution of the texture and $\tilde{A}_s$ the contribution of the speckle component. It is commonly assumed that $\tilde{A}_t$ is real and corresponds to the square root of the RCS. The different models for SAR statistics are derived from various choices for distributions for $\tilde{A}_t$ and $\tilde{A}_s$ some of which lead to analytical solutions for amplitude and power [27].

Recent work has shown that the probability distributions (PDFs) of the power of both PS and clutter pixels are non-Gaussian and can be described by several of the aforementioned SAR backscatter models, and that these models apply over varying bandwidths as well [29]. We choose an appropriate distribution by fitting a distribution function to the normalized power histogram of the dataset; this process is described in detail in Section III.

As an example of an application of these distributions, once known, the theoretical SCR distribution can be derived from (1). The derivation for the integrable expression for (1) is presented in [18]. Substituting random variables for the constants in (1), such that $P_d \sim p_d(x)$, $P_c \sim p_c(x)$, $P_n \sim p_n(x)$, and that $P_{cn} = P_c + P_n$ where $P_{cn} \sim p_c * p_n = p_{cn}(x) = \int_{-\infty}^{\infty} p_c(x-y)p_n(y)dy$. Then the distribution of (1) can be written

$$\begin{aligned} p(\gamma) &= \int_0^\infty x \cdot p_d(\gamma x) p_{cn}(x) dx \\ &= \int_0^\infty x \cdot p_d(\gamma x) \left[\int_{-\infty}^{\infty} p_c(x-y) p_n(y) dy \right] dx. \end{aligned} \tag{3}$$

Further modifications to (1) can be made to reflect other systems effects such as decorrelation, but the general form as indicated can be obtained once the distributions for PS and clutter statistics are known.

III. Data

We examine data from *X*-band (COSMO-SkyMed, $\lambda = 3.22$ cm), *C*-band (Sentinel-1 A, $\lambda = 5.66$ cm), and *L*-band (ALOS, $\lambda = 23.6$ cm) radar sensors over the Kilauea crater in Hawaii, which is natural terrain but mostly unvegetated, composed primarily of lava. The surface thus contains many stable pixels for our analysis and also allows us to evaluate the suitability of our fits and resulting model on natural terrain, as previous work has analyzed PS density over more structured terrain with manmade objects such as roads and buildings. The selected area is shown in Fig. 1, and important satellite parameters for the selected datasets are shown in Table I. The ALOS data are a mix of FBS and FBD mode data.

We only investigate single-polarization data, although the different single-pol types we have chosen (VV and HH) are due to limitations of the datasets. It is possible that this may affect the results of PS density, based on previous research that shows PS detection may be sensitive to polarization [30]; however, the same results have also shown that the larger distinction in between obtained PS densities is obtained when comparing between full-pol, dual-pol, and single-pol data rather than in between the two types of single-pol data. With respect to this work, it is assumed that the type of single-pol data utilized does not significantly affect the resulting PS density. Further study of polarization-dependent PS density remains an area of study for future work.

We also must consider the lack of calibration of the backscatter data across the three satellites. In other words, the scaling of the powers in all the data is different and arbitrary relative to one another. In theory, suitable distributions will fit the same

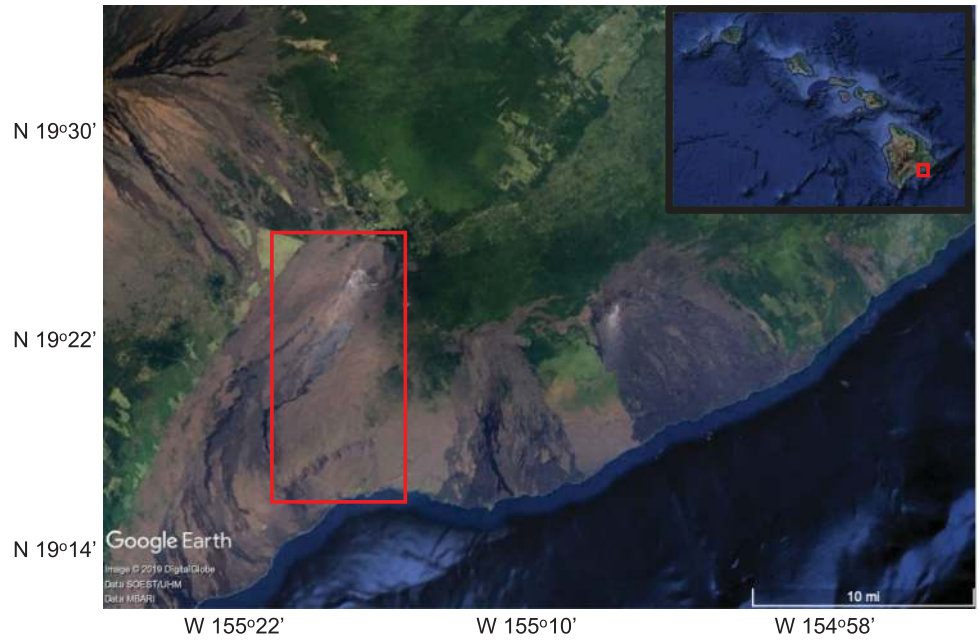

Fig. 1. Google Earth image of the selected imagery above the Kilauea crater with the selected area boxed in red. The inset shows the location of the area relative to the rest of the Hawaiian islands.

TABLE I
SATELLITE PARAMETERS

Parameter	Value		
Satellite	CSK-1	Sentinel-1A	ALOS
Wavelength	3.22 cm	5.66 cm	23.6 cm
Polarization	HH	VV	HH
Orbit pass direction	Descending	Descending	Ascending
Mode	H-Image	IW	FBS/FBD
Range	791 km	800 km	741 km
Pixel spacing in slant range	1.33 m	2.33 m	4.68 m/9.37 m
Bandwidth (range)	112.5 MHz	64.3 MHz	32.0 MHz
Look angle	40.59^o	31.72^o	22.19^o
Number of interferograms	96	91	56
Max spatial baseline	249.7 m	280.5 m	965.6 m
Max temporal baseline	464 days	204 days	965 days
Date range	8/2010-5/2011	11/2014-7/2015	5/2006-3/2011

data multiplied or divided by an arbitrary constant according to the scaling property of random variables. Because our main aim is to determine suitable distributions for the backscatter rather than exact parameters for these distributions, we proceed with a "naive" approach by scaling the magnitude of the power data so that they all have the same mean, arbitrarily chosen be the mean of the *C*-band (Sentinel) data, as the intermediate wavelength. We also briefly comment on the fits using different scaling constants.

IV. PS SELECTION AND PARAMETER FITTING

To select PS and clutter pixels in the dataset, we use the MLE method [16] to estimate the SCR of the pixels. This technique is fairly resistant to fluctuations in amplitude noise due to its phase-based approach. The general approach of the technique is as follows: first, an expression for the observed phase from each resel with respect to SCR is derived, and resels are assigned an SCR value from the maximum likelihood estimate given all the interferogram phase values. All resels with an SCR value higher than a certain threshold are assigned to be PS. In this work, we choose the threshold to be two to minimize false positives.

Once the PS and clutter pixels are distinguished, we form the empirical probability density function for the backscatter by computing the normalized histogram of the powers. We fit five common distributions: exponential, Weibull, K, lognormal, and G^0. While the lognormal does not result from the multiplicative model, it is included as it has been shown to empirically fit to data. We merely include the distribution here as a point of comparison. In this article, we define the distributions as follows:

Exponential:

$$f(x|\mu) = \frac{1}{\mu} e^{-\frac{x}{\mu}} \tag{4}$$

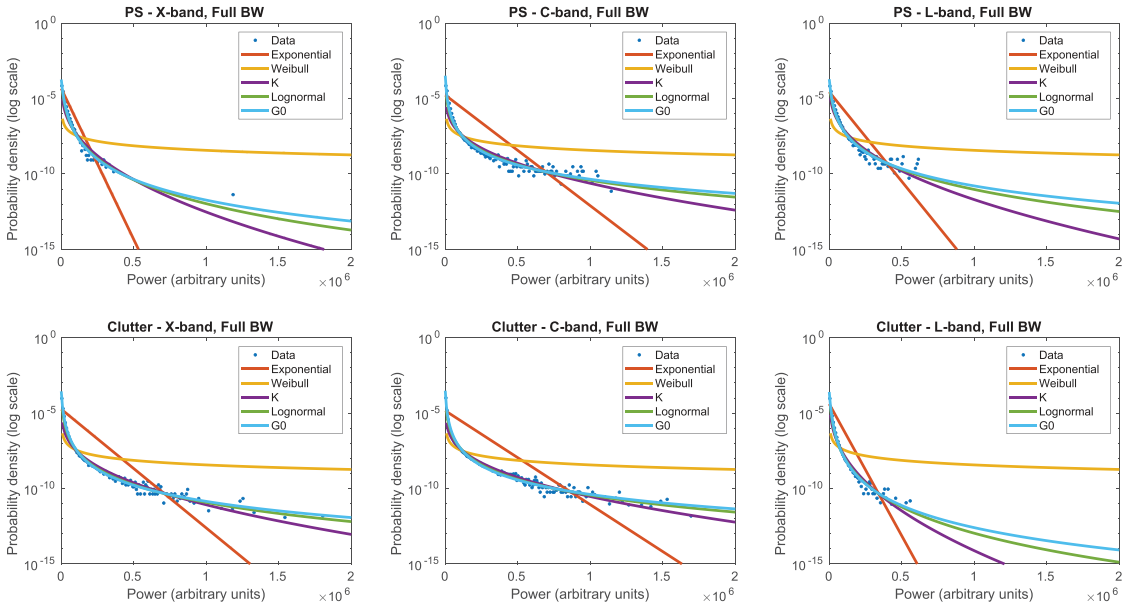

Fig. 2. Log scale plots of the five distributions fit the PS and clutter, respectively, for *X*-band (a, d), *C*-band (b, e), and *L*-band (c, f). All data have been scaled to the same mean, specifically the mean of the *C*-band (Sentinel) data.

Weibull:

$$f(x|a,b) = \frac{b}{a}\left(\frac{x}{a}\right)^{b} e^{-\left(\frac{x}{a}\right)^{b}} \tag{5}$$

Lognormal:

$$f(x|\mu,\sigma) = \frac{1}{x\sigma\sqrt{2\pi}} e^{\left(\frac{-(\log x-\mu)^2}{2\sigma^2}\right)} \tag{6}$$

K:

$$f(x|\alpha,\lambda) = \frac{2\lambda}{\Gamma(\alpha)}(\lambda x)^{(\alpha+1)/2-1} K_{\alpha-1}(2\sqrt{\lambda x}) \tag{7}$$

G^0*:*

$$f(x|\alpha,\gamma) = \frac{\Gamma(1+\alpha)}{\gamma^{-\alpha}\Gamma(\alpha)(\gamma+x)^{1+\alpha}} \tag{8}$$

where K is the modified Bessel function of the second kind. The K and G^0 distributions are defined according to [28]. Note that the G^0 is defined here for single-look images, and that we have reversed the sign of the parameter α so that all the parameters will be positive.

As in [29], we choose a simple fitting process: the fits were obtained using a constrained nonlinear solver to minimize the root mean square logarithmic error (RMSLE) which is defined as

$$\text{RMSLE} = \sqrt{\frac{\sum_{i=1}^{N}(\log \hat{y}_i - \log y_i)^2}{N}} \tag{9}$$

where y_i are the histogram values, $\hat{y}_i$ are the fit values, and N is the total number of points in the histogram. Because the empirical histograms of the data contain many bins with low values, particularly at bright pixels, we find that using the logarithmic (relative) error rather than the absolute error significantly improves the fit. More sophisticated parameter estimate procedures such as the ML and EM methods [31] can also be used, which may also be more effective in dealing with problems associated with scaling, as described. However, this is reserved for future work. Our initial results show that this straightforward method to fit the overall shape produces good results in determining which distributions are suitable for fitting PS and clutter.

TABLE II
RMSLE OF PS AND CLUTTER FITS

	PS			Clutter		
	X	C	L	X	C	L
Exp.	0.873	3.404	0.824	1.318	3.172	1.231
Wbl.	0.902	2.802	0.735	0.738	2.940	0.638
K	**0.841**	0.956	**0.714**	0.713	0.655	**0.600**
Logn.	0.955	**0.686**	0.787	**0.658**	**0.509**	0.631
G^0	**0.843**	**0.608**	**0.708**	**0.638**	**0.519**	**0.569**

Bolded values indicate the lowest two RMSLE fit values out of the five fits.

V. RESULTS AND DISCUSSION

A. *Fits to PS and Clutter Backscatter*

The initial fits for PS and clutter probability distributions for each wavelength at full bandwidth are plotted in Fig. 2, displayed on a log scale. Clearly, for all cases, the exponential and Weibull are poor fits while the K, lognormal, and G^0 distributions all visually conform well to the observed power histograms.

To more closely analyze the quality of fit to each distribution, we can examine the final RMSLE values resulting from each of the fits, shown in Table II. The errors are consistent with the observed trends in Fig. 2, where the K, lognormal, and G^0 distributions provide the best fits to both PS and clutter across

TABLE III
FITTED G^0 PARAMETERS FOR PS AND CLUTTER

	PS			Clutter		
	X	C	L	X	C	L
α	3.695	2.140	2.861	2.590	2.206	3.977
γ	$2.019 \cdot 10^4$	$6.561 \cdot 10^3$	$1.493 \cdot 10^4$	$9.384 \cdot 10^3$	$7.219 \cdot 10^3$	$1.584 \cdot 10^4$

different wavelengths. The K distribution provides a good fit to the PS backscatter at *X*- and *L*-band and the clutter backscatter at *L*-band, while the lognormal better fits the PS backscatter at *C*-band and the clutter at *X*- and *C*-bands. Meanwhile, the G^0 consistently provides the best or second best fit across all wavelengths for both PS and clutter.

Overall, it is clear that the G^0 distribution is the natural choice for both scatterer types as it provides the best overall fit. The fitted parameters for the distribution [the parameters as they are defined in (9)] are shown in Table III. The PS and clutter parameters are distinct from each other at all wavelengths. Both α and γ are larger for clutter points than PS points at *C*- and *L*-band, but the reverse is true at *X*-band. More research is required to further interpret the physical meaning and how they might relate to scattering mechanisms.

One caveat we have found when we have investigated the fits is that the fit is sensitive to some large scaling factors. When we apply the same scaling factor but divided by 100, the γ parameter scales by the 1/100 factor, and the α parameter remains the same, which is the expected behavior. However, when we apply the same scaling factor but multiplied by 100, both parameters change more dramatically. When examining the resulting plots, we observe that the shape of many of the fits change, but importantly, the same distributions generally still seem to fit well to each scatterer type across the wavelengths. This suggests that our fitting routine becomes slightly unstable for data that are either too large, spread out, or low in density. It is clear that improved fitting methods are required for the fits to be applicable across a larger range of data scaling. The important result, however, is that the same distributions (K, lognormal, and G^0) still fit well to the data.

Overall, although the fitting routine can generally be improved to obtain the exact parameters with more accuracy, our results show that there is a consistent distribution for the power backscatter can be selected across wavelength for both PS and clutter.

B. Role of Land Cover Type in Observed Backscatter Distributions

Land cover is an important factor that affects observed SAR and InSAR statistics, particularly backscatter distributions and PS density. In this work, we have shown that the K, lognormal, and G^0 distributions are suitable to describe the backscatter of PS and clutter over natural terrain that is primarily composed of bare, unvegetated land and includes a small amount of vegetated shrubland, forest, and grassland, with the G^0 distribution providing the lowest error fit. The G^0 distribution has also previously been shown to be appropriate fits for PS and clutter backscatter in urban, rural, and mixed urban/rural terrain, which exhibit heavier-tailed behavior than in areas of entirely natural terrain as they contain man-made structures that are stronger scatterers [29]. PS and clutter statistics in more diffusely scattering natural terrain has yet to be studied. However, we expect the G^0 distribution to still be applicable for both scatterer classes over a diverse set of land cover types, including more vegetated terrain, based on previous work that has shown that the distribution can describe high-resolution radar backscatter from forested areas [28]. Other studies have shown that the lognormal and K distributions may also still be appropriate fits for more vegetated regions [23], [32]. We expect these results to be applicable to both PS and clutter, but a more detailed study of PS and clutter distributions with respect to land cover type remains for future work.

C. Role of Other System Parameters in Observed Backscatter Distributions

Our results demonstrate the generalizability of several distributions for PS and clutter across appropriately scaled data from systems operating at different wavelengths. Other key system parameters that are expected to affect the resulting observed PS and clutter distributions include polarization mode and resolution (previous works have shown that backscatter angle can affect the observed distributions, but in spaceborne geometries the angle will not differ significantly across various systems).

The transmitter and receiver polarization mode has previously shown to have some effect on the detected PS density and type of detected point, as cross-polarization modes tend to be more sensitive to multiple-bounce surfaces, but our data in this study are limited to the single-pol HH and VV cases. We have shown that the studied distributions seem to describe both the HH and VV datasets equally well. However, more research is required to understand the generalizability of the distributions studied in this work to PS and clutter backscatter for the cross-pol cases as well as any differences between the HH and VV modes. This becomes particularly significant with respect to datasets of more diverse land cover, such as forest canopies.

Image resolution also directly affects the observed PS density as well as the shape of the backscatter distribution; however, the studied distributions have shown to be generalizable across various image resolutions [18], [29]. We note that in this study, each satellite has a different native resolution. We therefore briefly examine whether the differences in between the fitted parameters by wavelength may be due to the differing resolution of the data. For simplicity, we reduce the resolution in 1 D only; this is achieved by downsampling each raw SLC in range by

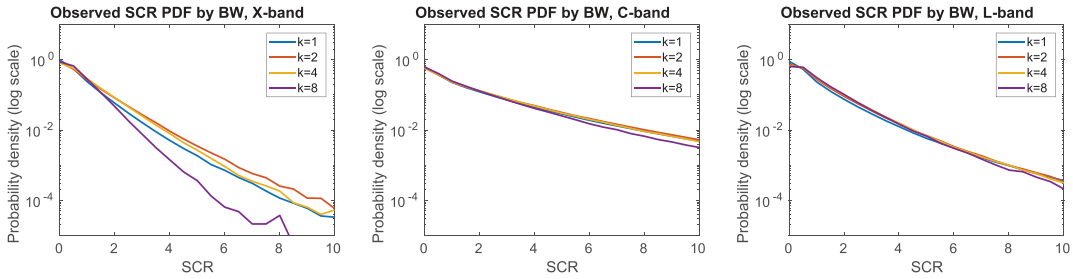

Fig. 3. Observed SCR distribution for downsampling factors of k = 1, 2, 4, and 8 at (a) *X*-band, (b) *C*-band, and (c) *L*-band.

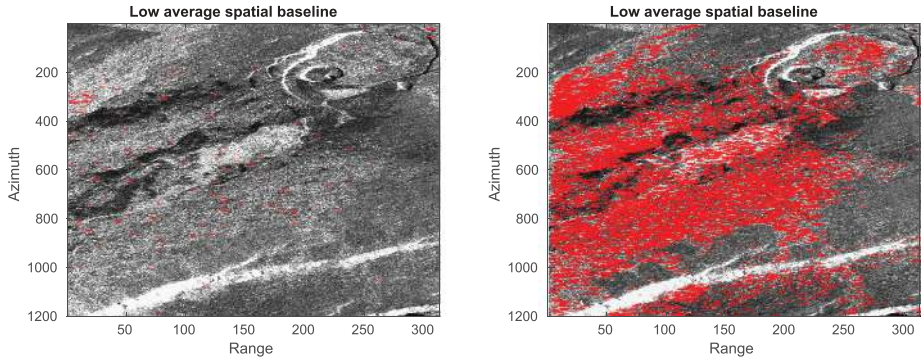

Fig. 4. Labeled PS (red points) for the defined region from CSK imagery for (a) high average spatial baseline and (b) comparatively lower average spatial baseline; clearly, a well-controlled baseline is critical for effective PS studies.

a factor of $k = 1, 2, 4,$ and 8 before forming the interferograms and selecting PS. The downsampling process used is described in detail in [18]. The resulting plots at each wavelength are shown in Fig. 3.

At each wavelength, there is a slight drop in the probability density at higher SCR values at the lowest bandwidth, $k = 8$, i.e., the probability of PS occurrence decreases for lower resolution, a trend which is most noticeable at *X*-band. However, the fundamental shape of the SCR distribution still appears to be dictated by the wavelength itself. This suggests that there are fundamental characteristics at each wavelength rather than resolution alone that contribute more strongly to the resulting observed PS density, which includes the distribution of the RCS that we fitted in the previous section. Additionally, the differences in the wavelengths may be due to other effects, such as decorrelation, which is considered briefly next.

D. Decorrelation as a Wavelength-Dependent Effect

Decorrelation is an important wavelength-dependent factor that we have not yet commented on. While there exist many PS identification methods that take into account SLC statistics [16], [33], decorrelation is generally recognized as an important part of InSAR analysis and must be included for accurate characterization of interferograms [20], [34]. Notably, Lien[19] incorporated decorrelation effects in PS selection and showed greater accuracy than previous methods in which decorrelation was not considered.

In this work, our PS detection scheme relied on SLC statistics rather than interferogram statistics, and as a result, we did not take into account decorrelation statistics, which changes with satellite and wavelength. However, we note that the results for PS density by wavelength in the previous section show the lowest PS density at all bandwidths for *X*-band data, while *C*-band data show the highest PS density. This is an interesting observation especially because data at *X*-band suffers the most from decorrelation noise, and Sentinel data in particular have the most well-controlled temporal and spatial baselines of the dataset. Therefore, decorrelation is an important factor that must be considered for future work in general.

A simple example using our data illustrates the importance of well-controlled baselines in PS studies, shown in Fig. 4. Both are derived from SAR images from the COSMO-SkyMed satellite (critical baseline: 12 400 m) and have been downsampled by 8 to a bandwidth of 14.1 MHz. However, the average spatial baseline is Fig. 4(a) is 604.7 m, while that of Fig. 4(b) is 130.8 m. Furthermore, the maximum spatial baseline of Fig. 4(a) is 1367 m, in contrast to Fig. 4(b), where the maximum spatial baseline is 249 m.

It is clear that contrary to some previous simplified assumptions about PS, many of these points are not entirely resistant to the effects of decorrelation. Additionally, research has attested that PS can, in fact, fade [35]. Therefore, especially when considering wavelength-dependent behavior, it is important to consider how decorrelation effects can be included when studying PS statistics and selection. This is an important avenue to include for future work.

VI. Conclusion

We have shown that several popular models for SAR backscatter are suitable for describing the power distributions of both PS and clutter across wavelength in natural terrain, and the G^0 distribution has shown to be to most suitable model for both scatterer types. With knowledge of these distributions, we can already design improved PS selection mechanisms. This comprises an important component of further developing PS detection theory; as briefly alluded to in the article, these distributions can also be used to develop a theoretical model for the distribution of PS density.

Another key factor that has not yet been considered is the role of polarization in PS density—namely, whether there is a significant difference in VV and HH polarizations with changes in bandwidth and wavelength. In this work, single-polarization data were used, but the Sentinel-1 A data were the only one of the dataset that was VV polarization rather than HH polarization.

Additionally, further future work will focus on linking the characteristics of PS and clutter to the underlying multiplicative model which will give further insight to the physical meaning of the fitted parameters, and finally apply the framework to develop improved PS detection algorithms. In general, this analysis could also be extended to clutter detection as there has recently been increased interest in exploiting the limited correlation of distributed scatterers to extract deformation, enabling analysis in particularly difficult areas.

Acknowledgment

COSMO-SkyMed data were provided by the Italian Space Agency (ASI) by means of the searchable catalog hosted by UNAVCO through the Supersites project organized by the Group on Earth Observations with ESA and other space agencies. Copernicus Sentinel data 2014–2015 were provided by the Alaska Satellite Facility Distributed Active Archive Center (ASF DAAC), accessed April 29, 2019 from https://asf.alaska.edu. ALOS data, JAXA/METI ALOS PALSAR L1.0 2006–2011, were also provided by the ASF DAAC, accessed April 29, 2019 from https://asf.alaska.edu.

References

[1] M. Moro *et al.*, "New insights into earthquake precursors from InSAR," *Scientific Rep.*, vol. 7, no. 1, pp. 1–11, 2017.

[2] E. J. Fielding, S. S. Sangha, D. P. S. Bekaert, S. V. Samsonov, and J. C. Chang, "Surface deformation of North–Central Oklahoma related to the 2016 Mw 5.8 Pawnee earthquake from SAR interferometry time series," *Seismological Res. Lett.*, vol. 88, no. 4, pp. 971–982, 2017. [Online]. Available: http://srl.geoscienceworld.org/lookup/doi/10.1785/0220170010 https://pubs.geoscienceworld.org/srl/article/88/4/971-982/354124

[3] S. Plank, "Rapid damage assessment by means of multi-temporal SAR—A comprehensive review and outlook to Sentinel-1," *Remote Sens.*, vol. 6, no. 6, pp. 4870–4906, 2014. [Online]. Available: http://www.mdpi.com/2072-4292/6/6/4870

[4] Y. Zheng, "Imaging Cascadia slow slip events with modern interferometric synthetic aperture radar datasets," Ph.D. dissertation, Dept. Geophysics, Stanford Univ., Stanford, CA, USA, 2019.

[5] A. Hooper, H. Zebker, P. Segall, and B. Kampes, "A new method for measuring deformation on volcanoes and other natural terrains using InSAR persistent scatterers," *Geophysical Res. Lett.*, vol. 31, no. 23, pp. 1–5, 2004.

[6] U. Wegmüller, D. Walter, V. Spreckels, and C. L. Werner, "Nonuniform ground motion monitoring with TerraSAR-X persistent scatterer interferometry," *IEEE Trans. Geosci. Remote Sens.*, vol. 48, no. 2, pp. 895–904, Feb. 2010.

[7] G. Luzi, M. Crosetto, and E. Fernández, "Radar interferometry for monitoring the vibration characteristics of buildings and civil structures: Recent case studies in Spain," *Sensors (Switzerland)*, vol. 17, no. 4, 2017, Art. no. 669.

[8] T. ElGharbawi and M. Tamura, "Estimating deformation due to soil liquefaction in Urayasu city, Japan using permanent scatterers," *ISPRS J. Photogrammetry Remote Sens.*, vol. 109, pp. 152–164, 2015.

[9] G. E. Hilley, R. Bürgmann, A. Ferretti, F. Novali, and F. Rocca, "Dynamics of slow-moving landslides from permanent scatterer analysis," *Science*, vol. 304, no. 5679, pp. 185–190, 2004.

[10] A. Hooper, P. Segall, and H. Zebker, "Persistent scatterer interferometric synthetic aperture radar for crustal deformation analysis, with application to Volcán Alcedo, Galápagos," *J. Geophysical Res.*, vol. 112, no. B7, 2007, Art. no. B07407. [Online]. Available: http://doi.wiley.com/10.1029/2006JB004763

[11] M. Crosetto, O. Monserrat, R. Iglesias, and B. Crippa, "Persistent scatterer interferometry: Potential, limits and initial C-and X-band comparison," *Photogrammetric Eng. Remote Sens.*, vol. 76, no. 9, pp. 1061–1069, 2010.

[12] S. Gernhardt, N. Adam, M. Eineder, and R. Bamler, "Potential of very high resolution SAR for persistent scatterer interferometry in urban areas," *Ann. GIS*, vol. 16, no. 2, pp. 103–111, 2010.

[13] M. Crosetto, O. Monserrat, M. Cuevas-González, N. Devanthéry, and B. Crippa, "Persistent scatterer interferometry: A review," *ISPRS J. Photogrammetry Remote Sens.*, vol. 115, pp. 78–89, 2016. [Online]. Available: http://dx.doi.org/10.1016/j.isprsjprs.2015.10.011

[14] M. Simons and P. A. Rosen, "Interferometric synthetic aperture radar geodesy," *Treatise Geophys.*, vol. 3, pp. 391–446, 2007. [Online]. Available:http://linkinghub.elsevier.com/retrieve/pii/B9780444527486000596

[15] B. M. Kampes and N. Adam, "The STUN algorithm for persistent scatterer interferometry," in *Proc. FRINGE*, 2005, pp. 1–14.

[16] P. S. Agram and H. Zebker, "Persistent scatterer selection using maximum likelihood estimation," *Geophysical Res. Lett.*, vol. 34, no. 22, 2007, Art. no. L22301.

[17] N. Adam, B. Kampes, and M. Eineder, "Development of a scientific permanent scatterer system: Modifications for mixed ERS/Envisat time series," in *Proc. Envisat ERS Symp.*, 2004, vol. 572, pp. 73.1–73.9.

[18] S. Huang and H. A. Zebker, "Persistent scatterer density by image resolution and terrain type," *IEEE J. Sel. Topics Appl. Earth Observ. Remote Sens.*, vol. 12, no. 7, pp. 2069–2079, 2019. [Online]. Available: https://ieeexplore.ieee.org/document/8641346/

[19] J. Lien, "Partially correlated persistent scatterer theory and techniques for radar interferometry," Ph.D. dissertation, Dept. Elect. Eng., Stanford Univ., Stanford, CA, USA, 2015.

[20] A. Ferretti, A. Fumagalli, F. Novali, C. Prati, F. Rocca, and A. Rucci, "A new algorithm for processing interferometric data-stacks: SqueeSAR," *IEEE Trans. Geosci. Remote Sens.*, vol. 49, no. 9, pp. 3460–3470, Sep. 2011.

[21] G. V. Trunk, "Radar properties of non-Rayleigh sea clutter," *IEEE Trans. Aerosp. Electron. Syst.*, vol. AES-8, no. 2, pp. 196–204, Mar. 1972. [Online]. Available: http://ieeexplore.ieee.org/document/4102929/

[22] G. Goldstein, "False-alarm regulation in log-normal and Weibull clutter," *IEEE Trans. Aerosp. Electron. Syst.*, vol. AES-9, no. 1, pp. 84–92, Jan. 1973. [Online]. Available: http://ieeexplore.ieee.org/lpdocs/epic03/wrapper.htm?arnumber=4103085

[23] J. K. Jao, "Amplitude distribution of composite terrain radar clutter and the K-distribution," *IEEE Trans. Antennas Propag.*, vol. 32, no. 10, pp. 1049–1062, Oct. 1984.

[24] K. Ward, "Compound representation of high resolution sea clutter," *Electron. Lett.*, vol.17, no. 16, pp. 561–563, 1981. [Online]. Available: http://ieeexplore.ieee.org/ielx5/2220/4245861/04245869.pdf?tp=&arnumber=4245869&isnumber=4245861ber=4245869

[25] F. Ulaby, F. Kouyate, B. Brisco, and T. H. Williams, "Textural information in SAR images," *IEEE Trans. Geosci. Remote Sens.*, vol. GE-24, no. 2, pp. 235–245, Mar. 1986. [Online]. Available: http://ieeexplore.ieee.org/document/4072450/

[26] H.-J. Mueller and R. Pac, "G-statistics for scaled SAR data," in *Proc. Geosci. Remote Sens. Symp.*, 1999, pp. 1297–1299.

[27] V. Anastassopoulos, G. A. Lampropoulos, A. Drosopoulos, and M. Key, "High resolution radar clutter statistics," *IEEE Trans. Aerosp. Electron. Syst.*, vol. 35, no. 1, pp. 43–60, Jan. 1999.

[28] A. Frery, H.-J. Muller, C. Yanasse, and S. Sant'Anna, "A model for extremely heterogeneous clutter," *IEEE Trans. Geosci. Remote Sens.*, vol. 35, no. 3, pp. 648–659, May 1997. [Online]. Available: http://ieeexplore.ieee.org/document/581981/
[29] S. Huang and H. A. Zebker, "SAR image statistics by bandwidth using a mixture distribution of persister scatterer and clutter distributions," in *Proc. IEEE Int. Geosci. Remote Sens. Symp.*, 2019, pp. 2965–2968.
[30] V. D. Navarro-Sanchez, J. M. Lopez-Sanchez, and L. Ferro-Famil, "Polarimetric approaches for persistent scatterers interferometry," *IEEE Trans. Geosci. Remote Sens.*, vol. 52, no. 3, pp. 1667–1676, Jul. 2014.
[31] X. Zhou, R. Peng, and C. Wang, "A two-component K-lognormal mixture model and its parameter estimation method," *IEEE Trans. Geosci. Remote Sens.*, vol. 53, no. 5, pp. 2640–2651, May 2015.
[32] A. P. Blake, D. Blacknell, and C. J. Oliver, "High-resolution SAR clutter textural analysis and simulation," in *Synthetic Aperture Radar and Passive Microwave Sensing*, G. Franceschetti, C. J. Oliver, J. C. Shiue, and S. Tajbakhsh, Eds., Bellingham, WA, USA: SPIE 1995, pp. 101–108. [Online]. Available: http://proceedings.spiedigitallibrary.org/proceeding.aspx?articleid=100 8645
[33] A. Ferretti, C. Prati, and F. Rocca, "Permanent scatters in SAR interferometry," *IEEE Trans. Geosci. Remote Sens.*, vol. 39, no. 1, pp. 8–20, Jan. 2001.
[34] M. Costantini, S. Falco, F. Malvarosa, F. Minati, F. Trillo, and F. Vecchioli, "Persistent scatterer pair interferometry: Approach and application to COSMO-skymed SAR data," *IEEE J. Sel. Topics Appl. Earth Observ. Remote Sens.*, vol. 7, no. 7, pp. 2869–2879, Jul. 2014.
[35] R. Brcic and N. Adam, "Detecting changes in persistent scatterers," in *Proc. IEEE Int. Geosci. Remote Sens. Symp.*, 2013, pp. 117–120.

Stacey Huang (Student Member, IEEE) received the B.S.E degree from Princeton University, Princeton, NJ, USA, in 2016 and the M.S. degree in electrical engineering from Stanford University, Stanford, CA, USA, in 2018. She is currently pursuing the Ph.D. degree in electrical engineering with Stanford University.

In 2016, she served as an Assistant Technical Staff with the Photonics Technology Department at The Aerospace Corporation, El Segundo, CA, USA. In 2019, she served as a Graduate Systems Engineering Intern with the MITRE Corporation, El Segundo, CA, USA. Her research interests include remote sensing, signal processing, and radar interferometry.

Ms. Huang was the recipient of the National Science Foundation's Graduate Research Fellowship Program (GRFP) and the Stanford Graduate Fellowship.

Howard A. Zebker (Life Fellow, IEEE) received the B.S. degree from the California Institute of Technology, Pasadena, CA, USA, in 1976, the M.S. degree from the University of California, Los Angeles, CA, USA, in 1979, and the Ph.D. degree in electrical engineering from Stanford University, Stanford, CA, USA, in 1984.

He is currently a Professor of Geophysics and Electrical Engineering with Stanford University, where his research group specializes in interferometric radar remote sensing. Originally, a Microwave Engineer, he built support equipment for the SEASAT satellite synthetic aperture radar and designed airborne radar systems. He later developed imaging radar polarimetry, a technique for measurement of the radar scattering matrix of a surface. He is best known for the development of radar interferometry, leading to spaceborne and airborne sensors capable of measuring topography to meter scale accuracy, and surface deformation to millimeter scale. More recently, he has been participating in the NASA Cassini Mission to Saturn, concentrating on analysis of data acquired by the radar/radiometer instrument.